Research Article

Deep Generative Modeling of Infrared Images Provides Signature of Cracking in Cross-Linked Polyethylene Pipe

Michael Grossutti, Joseph D'Amico, Jonathan Quintal, Hugh MacFarlane, W. Callum Wareham, Amanda Quirk, and John R. Dutcher*

Cite This: https://doi.org/10.1021/acsami.3c02564

Read Online

ACCESS | Metrics & More | Article Recommendations | Supporting Information

ABSTRACT: Hyperspectral infrared (IR) images contain a large amount of highly spatially resolved information about the chemical composition of a sample. However, the analysis of hyperspectral IR imaging data for complex heterogeneous systems can be challenging because of the spectroscopic and spatial complexity of the data. We implement a deep generative modeling approach using a β-variational autoencoder to learn disentangled representations of the generative factors of variance in a data set of cross-linked polyethylene (PEX-a) pipe. We identify three distinct physicochemical factors of aging and degradation learned by the model and apply the trained model to high-resolution hyperspectral IR images of cross-sectional slices of unused virgin, used in-service, and cracked PEX-a pipe. By mapping the learned representations of aging and degradation to the IR images, we extract detailed information on the physicochemical changes that occur during aging, degradation, and cracking in PEX-a pipe. This study shows how representation learning by deep generative modeling can significantly enhance the analysis of high-resolution IR images of complex heterogeneous samples.

KEYWORDS: hyperspectral infrared imaging, deep learning, representation learning, β-variational autoencoders, cross-linked polyethylene pipe
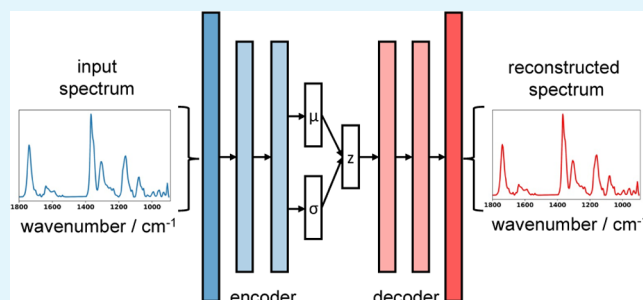
INTRODUCTION

Cross-linked polyethylene (PEX-a) pipe is increasingly used for domestic and industrial potable water transport and radiant heating and cooling applications. The cross-linking of polyethylene (PE) imparts favorable physical properties to the pipe such as high tensile strength. During in-service use, PEX-a pipe can be exposed to chlorine, elevated temperature, and UV light, which can induce thermo- and photo-oxidative degradation via free-radical pathways and PE chain scission. To enhance the long-term pipe durability, manufacturers typically include stabilizing additives such as primary antioxidants, secondary antioxidants, ultraviolet (UV) absorbers, and hindered amine light stabilizers. To evaluate their mechanical and oxidative resistance and forecast potential service lifetimes, PEX-a pipes are commonly subjected to hydrostatic pressure[1] and chlorinated water resistance[2] tests. As manufacturers of PEX-a pipe seek to expand the use of PEX pipe to newer and more vigorous operating conditions, they require tools for analyzing the mechanistic effects of the additional stresses on defects that can form and grow in the pipes, e.g., crack propagation.

Hyperspectral infrared (IR) imaging is a powerful tool for the study of aging, degradation, and cracking in PEX-a pipe. In a hyperspectral IR image, each pixel corresponds to an IR absorption spectrum. The IR absorption spectrum of PEX-a pipe contains extensive physicochemical information on the PE matrix, stabilizing additives, and aging and degradation products;[3-12] the high-spatial resolution of IR imaging enables the detailed examination of localized chemical changes that can occur, e.g., at the inner surface of the pipe wall and in the immediate vicinity of cracks. This highly spatially resolved physicochemical information has the potential to yield valuable insights into PEX-a pipe aging and failure.

However, the analysis of IR imaging data for complex heterogeneous systems, such as PEX-a pipe, can be limited by their inherent complexity. The information contained in hyperspectral IR images can be convoluted both spectroscopically and spatially. Spectroscopic complexity occurs because many covalent chemical bonds absorb IR light at multiple frequencies, and the absorptions often overlap to a significant degree for different chemical species. Spatial complexity arises from different chemical reactions that can occur simultaneously but to different extents at different locations within the
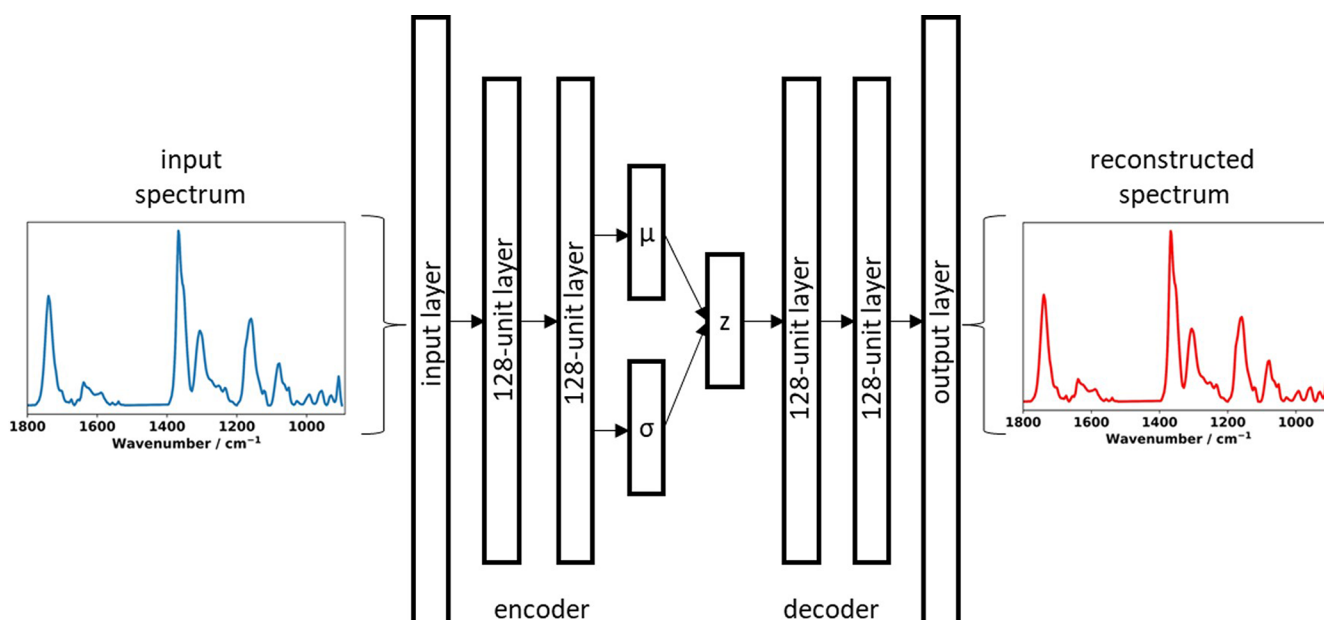
Figure 1. Schematic of the β-VAE model neural network architecture. The input and output layers are the original experimental and reconstructed IR spectrum, respectively. The encoder consists of two fully connected 128-unit layers with ReLu activations that encodes the input as a probability distribution parametrized by a 16-unit mean μ and standard deviation σ layer. The 16-unit sampling layer $z = \mu + \sigma \cdot \varepsilon$ serves as the input to the decoder. The decoder consists of two fully connected 128-unit layers with ReLu activations and a linearly activated output layer.

pipe, such as in the vicinity of the inner/outer wall surfaces or cracks. To extract as much information as possible from such data sets, it is necessary to implement advanced data analysis techniques.

Machine learning and deep learning approaches are increasingly being applied to spectroscopy data and material characterization.[13−19] We have previously reported on a deep learning approach that we applied to the study of complex IR spectroscopy data, in which we trained an artificial neural network β-variational autoencoder (β-VAE) on a data set of 25,000 IR spectra of PEX-a pipes.[5] β-VAEs are deep generative models capable of learning disentangled (independent and interpretable) representations of the generative factors responsible for variance in data.[5,20,21] For PEX-a pipe IR spectra, the physicochemical processes that can occur during pipe aging, degradation, and cracking are the underlying generative factors responsible for the variance in the spectra.[5] The β-VAE model learns disentangled representations of the physicochemical factors, in which each latent variable is sensitive to changes in a single physicochemical factor and insensitive to changes in others.

In this work, we apply a trained β-VAE model to a series of hyperspectral IR images of radial cross-sections of PEX-a pipe. The training of the β-VAE model was extended to a diverse data set of ~30,000 PEX-a pipe IR spectra from ~400 samples, including measurements on radial cross-sections of unused virgin pipe and used in-service pipe, both with and without cracking. We use the generative capacity of the trained β-VAE decoder neural network to demonstrate the physicochemical meaning of the learned representations. We then use the trained β-VAE encoder neural network to map the learned physicochemical factors to each pixel (spectrum) of the IR images. We show that the β-VAE model identifies distinct factors of aging and degradation and provides important information on the nature of crack formation and propagation in PEX-a pipes. Furthermore, the results illustrate the power

and potential of deep learning architectures in the analysis of complex hyperspectral data and should have important applications in other fields such as IR biomedical imaging.

■ MATERIALS AND METHODS

Sample Preparation. IR microscopy or IR imaging measurements were performed on virgin, aged, and in-service (both cracked and not cracked) PEX-a pipe cross-sections prepared by slicing the pipe samples perpendicular to the extrusion direction using either an American Optical model 820 rotary microtome or Epredia HM 355S microtome (slice thickness ~200 μm). Aged pipe samples were produced in-house using a custom recirculating water stress station[22] with distilled water at 80 psi and at temperatures between 70 and 90 °C. The stress station water was partially (~35%) replaced daily and completely replaced weekly. Cross-sectional slices were collected from small pipe segments (~3 cm length) at different time points during the aging process for measurement with IR microscopy.

Infrared Microscopy and Imaging Measurements. Transmission IR microscopy spectra were measured on a Thermo/Nicolet Continuum IR microscope equipped with a mercury cadmium telluride (MCT) detector at a spectral resolution of 4 cm^{-1}. Spectra were typically collected in 10−100 μm increments across the wall thickness of each pipe cross-section to obtain a radial profile. IR imaging measurements were performed at the Canadian Light Source (CLS) on an Agilent Cary 670 spectrometer equipped with a 128 × 128 pixel focal plane array detector at 25× magnification, 3.3 μm pixel size, and 4 cm^{-1} spectral resolution.

Spectra Preprocessing. Spectra were baseline corrected and normalized by the 2019 cm^{-1} band in Quasar[23] before further analysis. The 2019 cm^{-1} band arises from amorphous and crystalline regions of PE and is used as an internal standard to correct for variations in sample thickness.[3−5] The frequency regions selected for the deep learning analysis were 1800−1540 and 1400−898 cm^{-1}. These frequencies correspond to the fingerprint region of the IR spectrum, excluding the CH$_2$ bending region of PE, which is saturated for our sample thicknesses due to its strong absorbance.

β-VAE Model Architecture. Autoencoders are neural networks that are trained to copy their input to their output, typically in a restricted fashion via a dimensionally reduced encoded layer.[24] The information bottleneck imposed by the restriction forces the
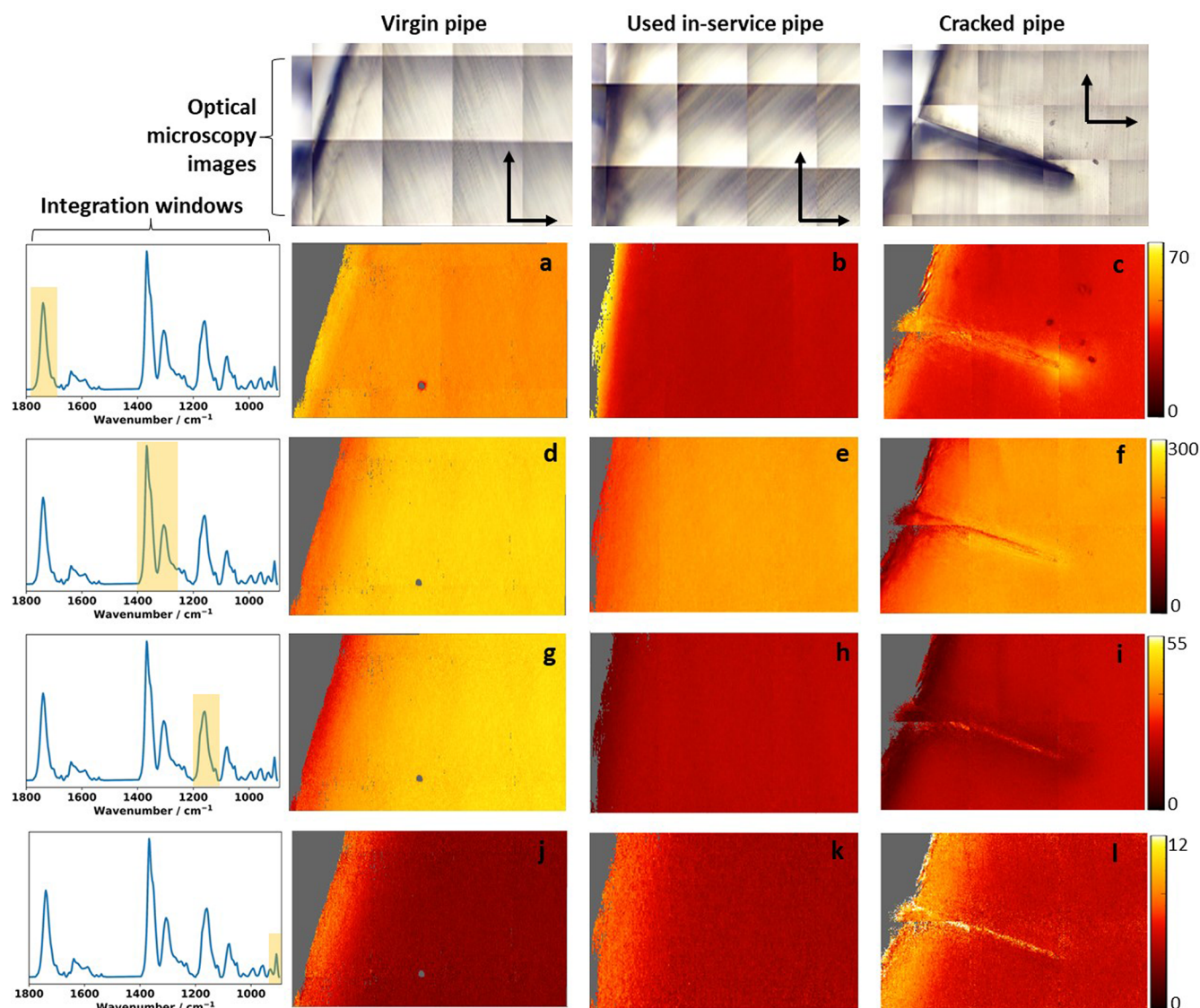
B

Figure 2. Collage of optical microscopy images and IR absorbance intensity maps of virgin, used in-service, and cracked PEX-a pipe cross-sections. The inner surface of the pipe wall is on the left of each image. The integration frequency windows used to generate the absorbance intensity maps for each row are shown as highlighted regions in the example IR spectrum. The integrated intensity windows for the four intensity maps are (a–c) 1800–1680, (d–f) 1400–1320, (g–i) 1200–1120, and (j–l) 915–900 cm^{-1}. For ease of visualization, the absorbance bands in the 1400–1200 cm^{-1} region are shown at 30% of their original intensity. The saturated bending CH_2 modes are omitted from the spectrum in the 1520–1400 cm^{-1} region. The scale bars in the optical microscopy images correspond to 200 μm.

autoencoder to prioritize the factors used to reconstruct the input, which can in turn force the model to learn useful properties of the data.[17] In this work, we implement a β-VAE to learn the generative factors of variance in our spectroscopic data set. The model architecture is illustrated in Figure 1. The β-VAE model can be viewed as consisting of two parts, an encoder neural network and decoder neural network.[20,21,24]

The encoder network encodes the input as random variables with a Gaussian probability distribution characterized by a mean μ and a standard deviation σ.[20,21] The decoder network sampled latent values, z, are obtained from this probability distribution via $z = \mu + \sigma \cdot \varepsilon$, where ε is a noise term that is generated by a random Gaussian distribution.[20,21] This reparameterization is necessary because the backpropagation of error required by neural network optimization algorithms cannot proceed through a random node.[20,21,24,25] The decoder then reconstructs the input from the sampled latent value z.

The β-VAE loss function minimized by the neural network optimizer is the sum of two components: the mean squared error (MSE) of the reconstruction compared to the input and a scaled Kullback–Leibler (KL) divergence term, where the KL divergence measures the difference between two probability distributions:[20,21,25]

$$\beta\_VAE_{loss} = MSE_{loss} + \beta \cdot KL_{divergence} \tag{1}$$

The MSE_{loss} component encourages the accurate reconstruction of the input spectrum. The $KL_{divergence}$ component acts as a regularizer on the encoded layer, encouraging the probability distribution of the latent variables (i.e., μ and σ) to resemble a random Gaussian distribution (defined by ε in the sampling operation). In β-VAEs, the $KL_{divergence}$ component is scaled by a hyperparameter coefficient β, as in eq 1.[20,21] Typically, $\beta > 1$, and it serves to increase the relative weight of the $KL_{divergence}$ term in the loss function.[20,21] The result is a balance, tuned by β, between the MSE_{loss} and $KL_{divergence}$ components. An informative learned latent dimension must contribute sufficiently to a reduction in the MSE_{loss} of the reconstruction such that it overcomes the corresponding (and inevitable) $KL_{divergence}$ cost. We note that, for a dimension to be informative, its μ and σ values must differ from the normal distribution and therefore incur a $KL_{divergence}$
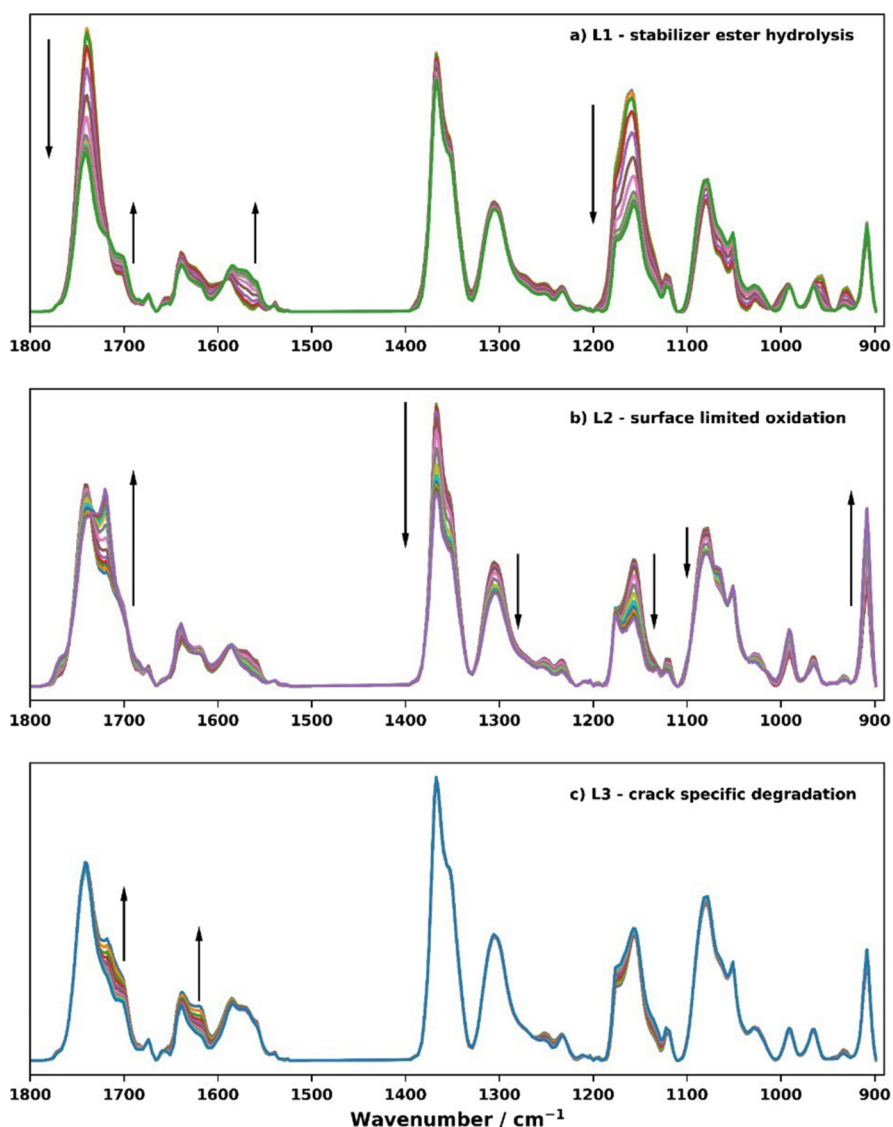
Figure 3. Decoder generated IR spectra of PEX-a pipe for latent dimension traversals of the (a) most informative latent dimension L1, the (b) second most informative latent dimension L2, and the (c) third most informative latent dimension L3. The arrows indicate the direction of change for the major peaks as the given latent dimension is traversed from negative to positive values. The absorbance bands in the 1400−1200 cm^{-1} frequency window are shown at 30% of their original intensity to clearly visualize changes across the entire spectrum. The saturated CH$_2$ bending modes, in the 1520−1400 cm^{-1} region, are omitted from the spectrum.

cost. For this reason, β-VAEs tend to be dimensionally efficient and not use more available latent dimensions than necessary.[20,21]

β-VAE Model Training and Hyperparameters. The β-VAE model was implemented in Python with TensorFlow[26] and Keras.[27] The input layer was 320-units, corresponding to an IR spectrum consisting of 320 data points. The encoder consisted of two fully connected 128-unit layers with ReLu activations. The latent dimension consisted of 16-units (16-unit mean and 16-unit standard deviation layer). The decoder consisted of two fully connected 128-unit layers with ReLu activations and a 320-unit output layer, corresponding to the reconstructed IR spectrum, with linear activations. The model was trained via k-fold cross-validation (k = 5) on a data set of ∼30,000 IR spectra from ∼400 samples of virgin, in-service, cracked, and aged PEX-a pipe using an Adam optimizer[28] with a learning rate of 10^{-4} and β = 10. The value of the crucial hyperparameter β was explored via a grid search and assessed by spectrum reconstruction and visual inspection of the latent space quality (see the Supporting Information for examples of experimental spectra and their corresponding reconstructions). We further assessed our choice of β by calculating a normalized value of β,

$\beta_{norm} = \frac{\beta \cdot latent\_size}{input\_size} = \frac{10 \times 16}{320} = 0.5$, which is consistent with that expected to give a disentangled latent space for our data and latent dimension size.[20]

RESULTS AND DISCUSSION

In Figure 2, we show optical microscopy images and hyperspectral IR imaging data for cross-sections of virgin, in-service, and cracked PEX-a pipe. IR spectroscopic studies of polyolefins often track the response of single IR peak intensities to a stressor (such as elevated temperature or UV exposure) as functions of time or pipe wall depth to characterize the chemical changes induced in the system.[29−35] In Figure 2, we show integrated intensity maps for four commonly characterized PE IR absorbance regions: 1800−1680, 1400−1320, 1200−1120, and 915−900 cm^{-1}. The dominant (but not necessarily exclusive) functional groups responsible for the IR absorbance in these regions are carbonyls, amorphous PE, ester group C−O linkages, and
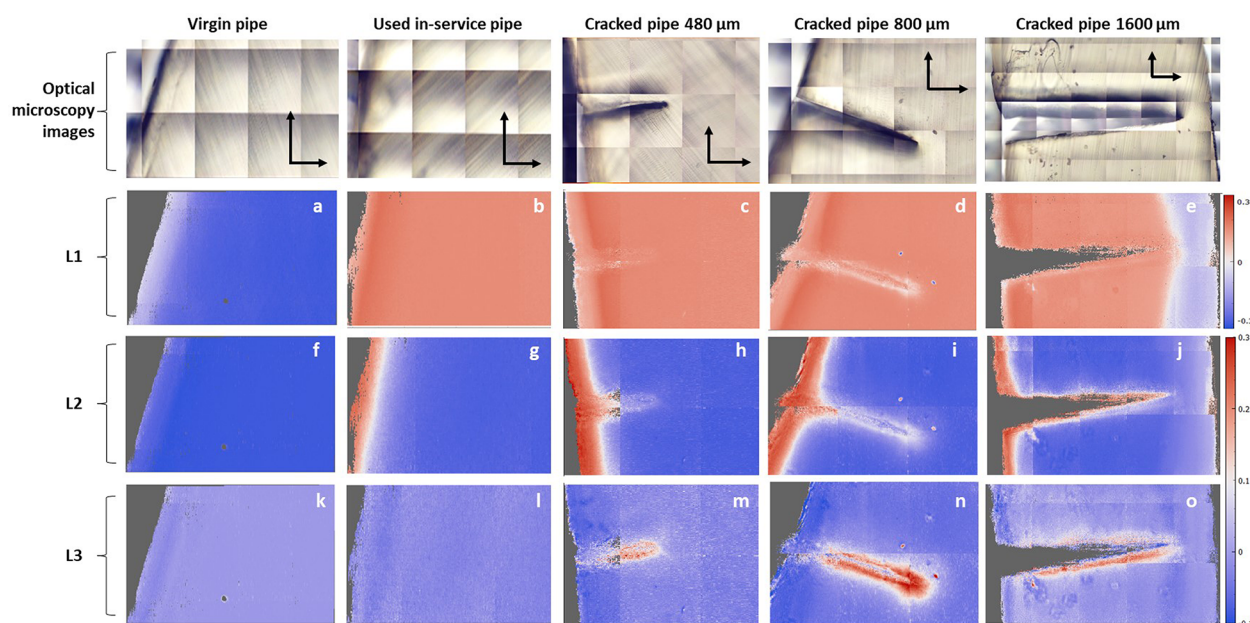
Figure 4. Collage of optical microscopy images (top row) and learned latent dimension heat maps of virgin, used in-service, and cracked PEX-a pipe for latent dimensions L1 (a−e), L2 (f−j), and L3 (k−o). The inner surface of the pipe wall is on the left of each image, and cracks extend from the inner surface into the pipe wall. The scale bars in the optical microscopy images correspond to 200 μm. The spectra (pixels) are filtered by a MSE of reconstruction threshold (MSE < 0.15) to remove noise from the images.

terminal vinyl unsaturations, respectively.[3−5] The intensity maps show the spatial distribution of the integrated absorbance intensity in these frequency windows for each of the three sample types.

The hyperspectra, as shown in Figure 2, capture the physicochemical state of the pipe as snapshots in time that contain information on aging, degradation, and cracking. However, it is difficult to identify and understand relationships between the mapped intensities in each frequency window, the different sample types (virgin, used, cracked), and specific features in the images, e.g., cracks and surfaces. For example, significant differences in absorbance are observed in the carbonyl region (Figure 2a−c) across sample types. The virgin sample exhibits strong and nearly uniform carbonyl region intensity. The used and cracked samples exhibit lower carbonyl contents compared to the virgin sample, yet regions close to the inner wall surface (left side of the image) and the crack (which extends into the pipe wall from the inner surface) display elevated carbonyl content relative to the surrounding regions. This suggests that multiple processes leading to carbonyl depletion and carbonyl growth can occur in the pipe during in-service use. The 1400−1320 cm^{-1} intensity maps (Figure 2d−f), dominated by amorphous PE bands, show subtle differences between sample types and differences between surfaces/cracks and the bulk. The 1200−1120 cm^{-1} intensity maps (Figure 2g−i) show dramatic differences between the virgin sample and those that have experienced in-service conditions. However, the used and cracked samples appear very similar. The terminal vinyl unsaturation intensity maps (Figure 2h−j) all show elevated vinyl content near the surface, and the in-service samples show elevated levels in the bulk compared to the virgin sample. In summary, patterns and relationships between spectral regions, sample types, and image features cannot readily be identified and analyzed by examining data representations such as these intensity maps.

The absorbance intensity maps in Figure 2 show the spatial distribution of different functional groups in the samples. Although this representation of the data is useful for visualizing common metrics like carbonyl or terminal vinyl content, these metrics do not necessarily align with the generative factors of variance in the data, which can make their interpretation difficult.[4,5,20,36] In contrast, disentangled data representations tend to align with the data generative factors and are independent and interpretable.[5,20,21] β-VAEs are a class of deep learning models that are excellent at learning disentangled data representations.[5,20,21] We have previously trained a β-VAE on a diverse data set of IR spectra of virgin, aged, in-service, and cracked PEX-a pipe.[5] In the present study, we have expanded the size and IR frequency window of our training data set to train and tune a new β-VAE model on this larger data set. The result is an updated model that is very similar to that described in ref 5 but now contains more information obtained by expanding the spectral range to include absorptions in the 1400−1200 cm^{-1} region, which are associated with the CH$_3$ bending and CH$_2$ wagging modes of amorphous PE. The trained β-VAE model consists of an encoder that can compress new data to the lower dimensional latent space of learned (disentangled) representations and a decoder that can generate new spectra from the latent space. We use both the encoder and decoder to analyze new data and to understand the physicochemical meaning of learned latent representations.

In Figure 3, we show the IR spectra generated by the decoder by individually traversing the three most informative latent dimensions, i.e., those with the largest KL divergences, holding all others constant (see the Supporting Information for all latent dimension traversals). In this way, we can understand the spectroscopic and physicochemical meaning of the individual latent dimensions. The arrows indicate the direction of change for the major peaks as the given latent dimension is traversed from negative to positive values. In Figure 3a, we

show the spectra generated by traversing the most informative latent dimension L1. To show the spectral changes most clearly, the L1 traversal is initialized using the latent coordinates for a virgin pipe spectrum. As L1 is traversed from negative to positive values, the absorbance peaks at 1740 and 1170 cm^{-1}, corresponding to ester C=O and C−O groups, undergo large decreases, while peaks at 1700 and 1570 cm^{-1}, corresponding to carboxylic acid C=O and carboxylate COO$^-$ groups, increase in intensity.[4,5] These changes are consistent with hot water-driven hydrolysis of stabilizing additive ester linkages, as observed in previous studies.[4,5,37−42] In Figure 3b, we show the spectra generated by traversing the second most informative latent dimension L2. The L2 traversal is initialized using the latent coordinates of a used in-service pipe spectrum. As L2 is traversed from negative to positive values, the absorbance peaks at 1720 and 908 cm^{-1} undergo large increases. These peaks correspond to major products of PE degradation: ketone carbonyl and terminal vinyl groups, respectively.[3,5] Major decreases occur in the 1400−1275 cm^{-1} region that is associated with the CH$_3$ bending and CH$_2$ wagging modes of amorphous PE and weaker decreases at 1080 cm^{-1} that is associated with the PE backbone C−C stretching modes.[43] Taken together, these changes are consistent with the oxidative degradation and chain scission of amorphous PE components of the PEX-a pipe matrix. In Figure 3c, we show the spectra generated by traversing the third most informative latent dimension L3. The L3 traversal is also initialized using the latent coordinates of a used in-service pipe spectrum. As L3 is traversed from negative to positive values, the absorbance peaks at 1720 and 1620 cm^{-1} increase in intensity with subtle changes elsewhere. These peaks are consistent with ketone carbonyl and conjugated alkene functional groups.[5]

The spectroscopic variance and physicochemical factors that underly the three most informative latent dimensions are very similar to those learned in ref 5 and correspond to stabilizing additive ester hydrolysis (L1), amorphous PE oxidation and chain scission (L2), and degradation characterized by the increased carbonyl and conjugated alkene content (L3), which is specific to cracks in PEX-a pipe as discussed below. An important improvement in the present model is the explicit identification of the loss of amorphous PE absorptions (as opposed to crystalline PE) in conjunction with the oxidation and chain scission captured by L2. The value of these learned representations becomes especially clear when we apply the encoder to new data not used in training, which include hyperspectral IR imaging data from virgin and used pipe, as well as pipe with cracks of different lengths.

In Figure 4, we show optical microscopy images and heat maps of the learned latent representations for cross-sections of virgin and used in-service pipe and pipe exhibiting cracks of different lengths. Each pixel in the heat maps corresponds to a single IR spectrum. To generate the heat maps, the trained encoder of the β-VAE model is applied to each spectrum in the IR images, and the corresponding latent value for each of L1, L2, and L3 is mapped to its (x, y) spatial coordinate. The heat maps show the spatial distributions of learned latent variables, with red corresponding to positive latent values and blue corresponding to negative latent values. The latent values correspond to the degree to which the learned representation of an underlying generative factor is present at a given (x, y) location. For all cases, blue (negative values) indicates the absence, and red (positive values) indicates the presence of the physicochemical factor. As the latent values become increasingly positive, the spectra increasingly differ from the spectra of virgin pipe that has yet to experience aging conditions, such as in-service use, where degradative processes occur. The hyperspectra are filtered by a MSE of reconstruction threshold (MSE < 0.15) to remove pixels that are not well described by the β-VAE model. This excludes data with generative factors that are very different from those learned during training. For our current data, which is well described by the β-VAE model, this is a convenient way of removing noise from the images. For example, the noisy spectra measured in the empty space of the gap in the large 1600 μm long crack are readily filtered out of the images in Figure 4e,j,o.

The spatial distributions of the latent values in Figure 4 are consistent with our understanding of their physicochemical meaning and previous studies: hydrolysis L1 pervades the interior bulk of the pipe, oxidative damage L2 is confined to regions adjacent to surfaces exposed to water, and crack-specific degradation L3 is confined to regions near cracks.[4,5] The heat maps are snapshots in time that capture the physicochemical state of the pipe. We can understand the progression of the physicochemical factors of aging and degradation in PEX-a pipe by more closely examining the behavior of L1, L2, and L3 between sample types and within individual samples.

We can examine the L1 row in Figure 4a−e to see the progression of stabilizing additive ester hydrolysis across the pipe wall thickness. For L1, the latent values range from about −0.3 to 0.3 for virgin and extensively hydrolyzed samples, respectively. The nearly uniform blue color in the virgin pipe L1 heat map (Figure 4a) indicates the absence of ester hydrolysis. The used in-service L1 heat map (Figure 4b) reveals nearly uniform and extensive hydrolysis, as do the L1 heat maps of pipe cracks in Figure 4c,d. Interestingly, in Figure 4e, in which there is a larger field of view, we can see that hydrolysis has progressed through almost the entire pipe wall thickness, but there remains a region near the outer surface that retains non-hydrolyzed additive (although the hydrolysis near the outer surface is greater than that in the virgin pipe). We note that the hydrolysis extends even further across the pipe wall thickness near the tip of the crack, with extensive cracking resulting in a more rapid advance of the hydrolysis front near the crack tip. This likely occurs because of the aqueous environment that accompanies the development and propagation of cracks.

The latent variable heat maps exhibit distinct localized variations with respect to distance from key physical features such as surfaces and cracks. We characterize these variations with sigmoidal functions and quantify the latent variable gradients with depth and width parameters. We investigate the additive hydrolysis behavior around the transition zone that is evident in Figure 4e. To quantify the gradient in the degree of hydrolysis, we consider a line profile of L1 pixels, locally perpendicular to the hydrolysis front, and fit this profile to a sigmoidal function. In Figure 5, we plot the L1 values as function of position within the profile (inset image in Figure 5). From the best fit to the sigmoidal function, the center of the hydrolysis transition zone is identified by the inflection point d_0, and the width of the transition is characterized by the width parameter $\Delta = 43$ μm. This gradient width likely reflects fundamental aspects of the complex hot water-driven second-order autocatalytic hydrolysis process[3] including the dependence of the reaction on temperature and diffusion. The trained
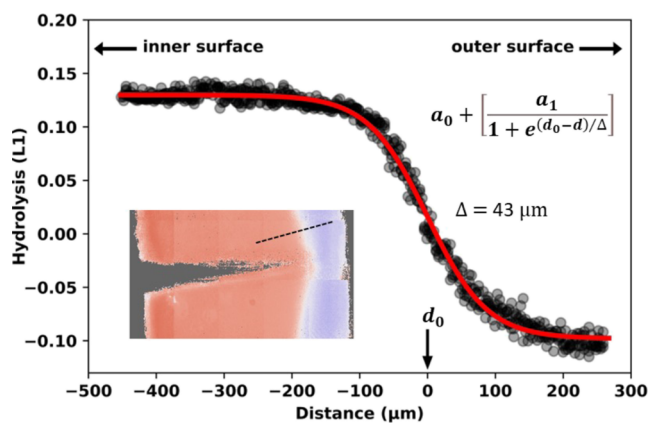
Figure 5. Hydrolysis profile (latent variable L1 versus distance) along dashed line in the inset image. The red line corresponds to the best fit to the sigmoidal function shown as an inset to the figure, characterized by a distance d_0 at the midpoint of the sigmoidal function of width Δ.

β-VAE model enables automated reproducible identification and quantification of this process.

For the L2 row heat maps in Figure 4f−j, the latent values range from about −0.1 to 0.3 for virgin and extensively oxidized samples, respectively. The regions near the inner wall surface of all samples exposed to in-service conditions exhibited elevated L2 values associated with oxidation, chain scission, and amorphous PE loss. In contrast, the virgin sample was uniform in color with low values of L2 (blue), indicating only low levels of degradation and suggesting that changes in L2 are associated with exposure to water in in-service conditions. We fit the variation in L2 with distance near the inner surface of pipes exposed to in-service conditions using a sigmoidal function. In Figure 6, we show L2 distance profiles for in-service and cracked samples. The profiles are well described by fits to a sigmoidal function, where the d_0 and Δ values correspond to the best-fit penetration depth and gradient width of the degradation front, respectively. For the selected profiles, d_0 varies between 68 and 171 μm and Δ varies between 30 and 49 μm. It is difficult to compare d_0 and Δ values between samples because the inner surfaces are degraded, poorly defined, and exhibit noisier spectra that do not meet the reconstruction quality threshold (MSE < 0.15). Nonetheless, the d_0 and Δ values for different samples have very similar values, relative to the scale of the pipe wall thickness (∼2 mm), and the values of the lower asymptotes (a_1) are nearly identical. The large, localized increases in the L2 values near the inner surface of all samples show that the degradation described by L2 is related to processes that occur at the inner surface. This, together with the absence of elevated L2 values at the outer surface of Figure 4j, shows that the L2 degradation processes are directly related to exposure to water flowing through the pipes. For the cracked samples (Figures 4h−j and 6b−d), we note that, with respect to the interior bulk of the pipe wall, the pixels adjacent to the cracks exhibit elevated L2 values and are positively correlated with crack length. Finally, we can see that, unlike additive hydrolysis described by L1 that penetrates deep into the pipe wall, the amorphous PE degradation L2 process is restricted to interfacial regions near surfaces that are directly exposed to water. The immediate surface degradation of amorphous PE in PE pipes has been observed before and may be due to highly reactive "superoxidant" species.[44]
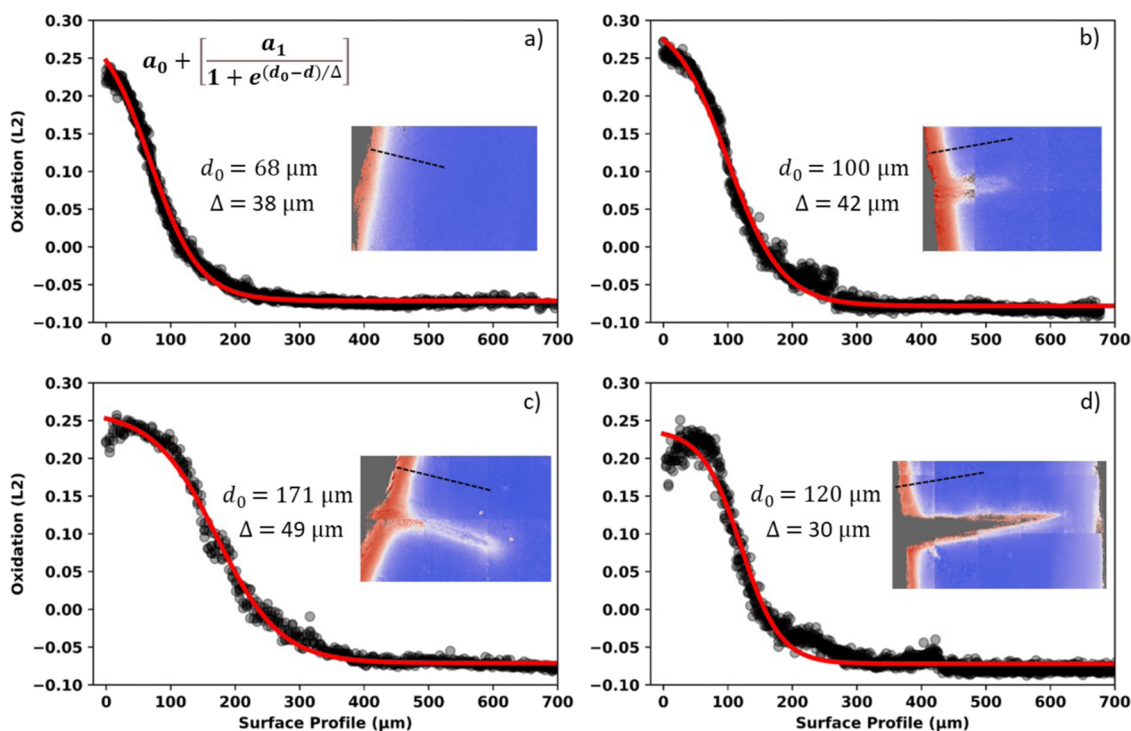

Figure 6. Variation of L2 latent variable values with distance measured locally perpendicular to degradation fronts (see the inset images) for (a) used in-service pipe ($r^2 = 0.994$), and pipes with cracks of length (b) 480 μm ($r^2 = 0.990$), (c) 800 μm ($r^2 = 0.992$), and (d) 1600 μm ($r^2 = 0.978$). The red curves correspond to the best fits of the profiles to the equation shown as an inset to part (a). The best fit values of d_0 and Δ are shown in the insets of each plot.
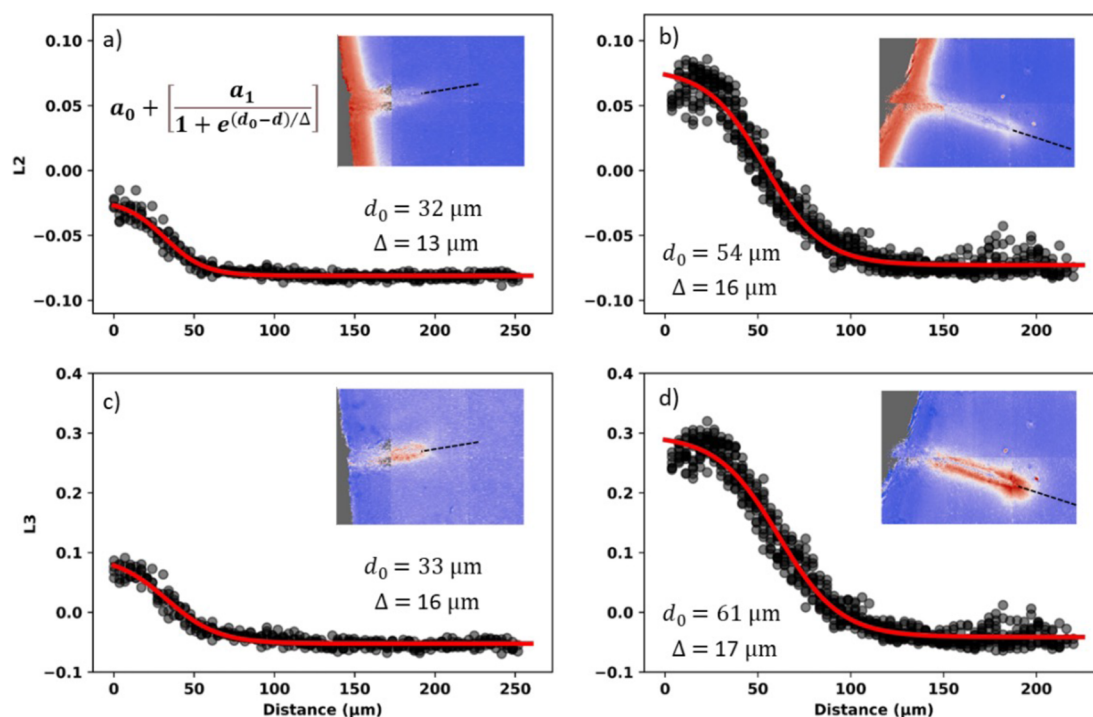
G

Figure 7. Variation of L2 and L3 latent variable values with distance measured along the crack propagation trajectory (see the inset images) for cracks of length (a,c) 480 and (b,d) 800 μm. The red curves correspond to the best fits [(a) $r^2 = 0.953$, (b) $r^2 = 0.969$, (c) $r^2 = 0.952$, and (d) $r^2 = 0.975$] of the profiles to the equation shown as an inset to part (a). The best fit values of d_0 and Δ are shown in the insets of each plot.
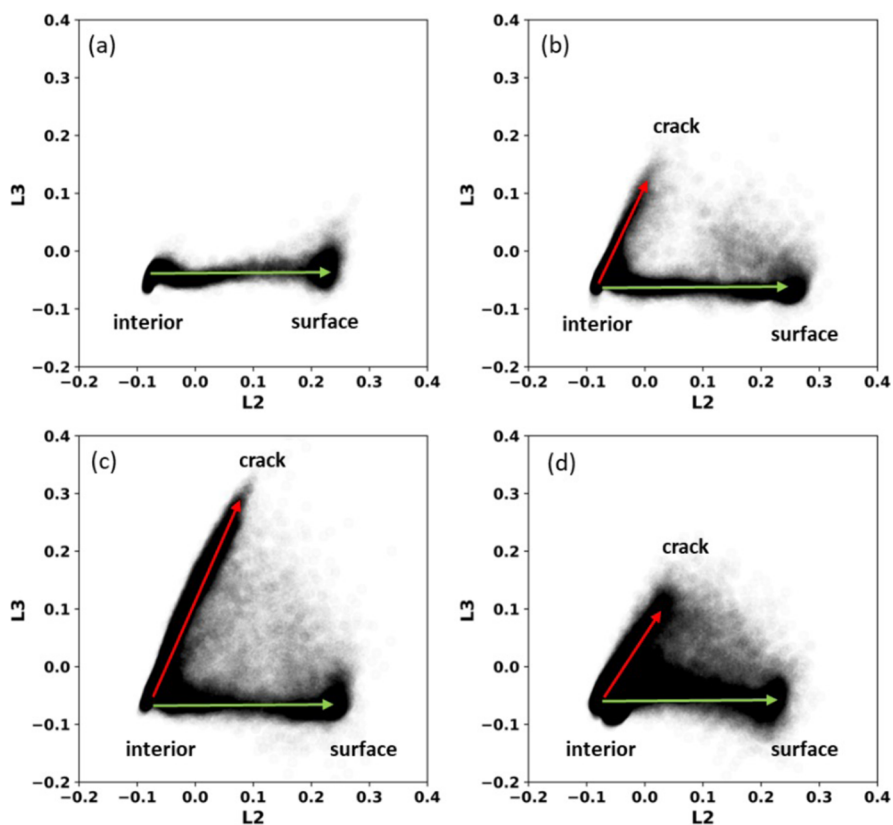

Figure 8. Two-dimensional (2D) latent encodings (L2 and L3) for the IR images of (a) used in-service pipes (Figure 4g,l) and pipes that exhibited cracks of length (b) 480 μm (Figure 4h,m), (c) 800 μm (Figure 4i,n), and (d) 1600 μm (Figure 4j,o). The symbols used to represent the data points are highly transparent to reveal the density of the data points and the trajectories of surface-associated degradation (green arrow) versus crack-associated degradation (red arrow).

We can better understand the physicochemical changes associated with crack formation and propagation by examining the L3 row heat maps, as shown in Figure 4k–o. For L3, the latent values range from about −0.1 to 0.3 for virgin and cracked regions, respectively. The virgin and used pipe L3 heat maps in Figure 4k,l are uniformly blue, corresponding to uniformly low levels of L3. The remaining heat maps (Figure 4m–o) show different stages of cracking, with elevated levels of L3 near the cracks: a short, early-stage crack (Figure 4m), a longer crack that has propagated nearly halfway through the pipe wall (Figure 4n), and a pipe with extensive cracking in which the crack has propagated ∼75% through the pipe wall (Figure 4o). The L3 heat map for the short, early-stage crack (Figure 4m) exhibits elevated values at the tip and, to some extent, along the length of the crack. For the medium length crack (Figure 4n), the L3 values at the tip and along the length of the crack are comparable with those for the short, early-stage crack. The longest, late-stage crack (Figure 4o) exhibits elevated L3 values along the length of the crack but with less intensity than that for the medium length crack. In all cases, the elevated L3 values do not extend all the way to the inner surface, reaching only ∼200 μm from the inner wall surface where the effects of oxidation (L2) are dominant. There are two possible explanations for this behavior: either extensive L2 oxidation at the inner surface has eliminated functional groups associated with L3 degradation, thereby obscuring its presence at an earlier stage of cracking, or the L3 degradation does not occur at the surface. Further work on earlier stage cracking will examine this point.

In Figure 7, we plot the variation of the L2 and L3 latent variable values with distance along the crack propagation trajectory, extended into the pipe wall from the leading edge of the crack, for the short, early-stage 480 μm long crack and the more advanced 800 μm long crack. The L2 and L3 profiles are well described by fits to a sigmoidal function, for which the d_0 and Δ values correspond to the best-fit penetration depth and gradient widths of the latent variables, respectively. The penetration depth values, d_0, range between 32 and 61 μm and are very similar across latent dimensions within each cracked sample. The gradient width values, Δ, range between 13 and 17 μm and are very similar across samples (i.e., the short, early-stage crack, and more advanced crack) and latent dimensions (i.e., L2 and L3). Interestingly, this shows that the penetration gradient of L2 and L3 into the pipe wall, ahead of the leading edge of the cracks, follows approximately the same distance dependence (despite the medium length crack being at a more advanced stage with significantly more intense L2 and L3 values than the short, early-state crack). This suggests that the degradation associated with the L2 and L3 generative factors can occur in the same regions and may act in concert with one another at the leading edge of a propagating crack.

In Figure 8, we represent the IR images of the in-service and cracked samples as two-dimensional latent encodings, by plotting L3 vs L2, which allows us to examine the relationship between L2 and L3 more closely. Figure 8a shows the (L2 and L3) representation of the used in-service sample (Figure 4g,l). The data trajectory is essentially parallel to the L2 axis because of the dominance of the L2 surface gradient discussed above (Figures 5 and 6). In Figure 8b, we see the emergence of a trajectory that runs nearly parallel to the L3 axis, which we associate with the presence of a short, early-stage crack. This trajectory also contains a small contribution from L2 (Figure 4h,m). In Figure 8c, for the medium crack, we see the

extension of the crack-associated trajectory (Figure 4i,n) to larger values for both L2 and L3, with the trajectory direction in the L2−L3 space nearly identical to that for the short, early-stage crack. We note that the density of points lying in the space between the surface-associated trajectory and crack-associated trajectory is larger for the medium crack than that for the short, early-stage crack. For the longest late-stage crack (Figure 8d), the crack-associated trajectory is less well defined with a substantial increase in the density of points lying between the crack-associated and the surface-associated trajectories. We suggest that this behavior occurs because, as the cracking becomes more extensive, the water flowing through the pipe penetrates the crack, resulting in surface-limited physicochemical changes associated with L2. As the physicochemical changes described by L2 progress, the physicochemical and spectral signature of L3 is lost. The "filling in" of the space between the two trajectories likely captures this process as the points migrate from L3 to L2. Although the increased ketone carbonyl and conjugated alkene content associated with L3 seems to be essential for cracking, the oxidation, chain scission, and amorphous PE loss described by L2 may also be an important contributor, which is consistent with the distance profiles quantified in Figure 7.

■ SUMMARY AND CONCLUSIONS

The application of a trained β-VAE model has significantly enhanced the analysis of the hyperspectral IR images, providing a comprehensive and highly spatially resolved representation of the physicochemical changes that can occur in PEX-a pipes during in-service use. The relationships between the latent variables L1, L2, and L3 near the cracks are especially informative. The stabilizing additive hydrolysis described by L1 is present throughout the bulk of all the in-service samples, regardless of the presence of cracks. Changes to L1 are associated with a detrimental aging process since stabilizing additives are oligomerized via ester linkages to inhibit their migration within the pipe wall, and cleavage of this linkage reduces their molecular weight and could lead to increased diffusive loss and reduced additive performance. Similarly, the oxidative degradation, PE chain scission, and amorphous PE loss described by L2 are present at the inner surface of all in-service samples, regardless of the presence of cracks. This can also be considered to be a detrimental degradative process, but it may not be a crucial contribution to cracking as it is also observed in samples without cracks. In contrast, the elevated ketone carbonyl and conjugated alkene content captured by L3 is only observed in the immediate vicinity of cracks. This suggests that the physicochemical changes described by L3 are necessary for crack progression. We note that elevated L2 values also occur near the cracks and appear to be coincident with increases in L3, and the two factors may be cooperatively responsible for crack propagation.

The high-spatial resolution tracking of physicochemical changes associated with aging, degradation, and cracking in PEX-a pipe that is enabled by the β-VAE analysis provides new insights into pipe stability and lifetime. It is our hope that this will provide PEX-a pipe manufacturers with a new tool—by tailoring the training of the β-VAE model to their specific additives, manufacturing history and stress-testing protocols, they will be able to extend the use of their pipes into ever more vigorous and challenging operating environments.

More generally, the results of the present study show how representation learning via deep generative modeling can be

I

used to extract meaningful and interpretable information from complex high-spatial resolution hyperspectral images, with the potential to extend the applications of IR imaging to other complex cases such as biomedical imaging.

ASSOCIATED CONTENT

Supporting Information

The Supporting Information is available free of charge at https://pubs.acs.org/doi/10.1021/acsami.3c02564.

> Detailed information on β-VAE reconstructions of experimental IR spectra and latent dimension traversals by the decoder network (PDF)

AUTHOR INFORMATION

Corresponding Author

John R. Dutcher − *Department of Physics, University of Guelph, Guelph, Ontario N1G 2W1, Canada;* ⊙ orcid.org/0000-0003-2594-5388; Phone: 519-824-4120 ext. 53950; Email: dutcher@uoguelph.ca

Authors

Michael Grossutti − *Department of Physics, University of Guelph, Guelph, Ontario N1G 2W1, Canada*

Joseph D'Amico − *Department of Physics, University of Guelph, Guelph, Ontario N1G 2W1, Canada*

Jonathan Quintal − *Department of Physics, University of Guelph, Guelph, Ontario N1G 2W1, Canada*

Hugh MacFarlane − *Department of Physics, University of Guelph, Guelph, Ontario N1G 2W1, Canada*

W. Callum Wareham − *Department of Physics, University of Guelph, Guelph, Ontario N1G 2W1, Canada*

Amanda Quirk − *Canadian Light Source Incorporated, Saskatoon, Saskatchewan S7N 2V3, Canada*

Complete contact information is available at:
https://pubs.acs.org/10.1021/acsami.3c02564

Notes

The authors declare no competing financial interest.

ACKNOWLEDGMENTS

REFERENCES

(1) *ASTM Standard D2837-13, Standard Test Method for Obtaining Hydrostatic Design Basis for Thermoplastic Pipe Materials or Pressure Design Basis for Thermoplastic Pipe Products*, 2013.

(2) *ASTM Standard F2023-15, Standard Test Method for Evaluating the Oxidative Resistance of Crosslinked Polyethylene (PEX) Pipe, Tubing and Systems to Hot Chlorinated Water*, 2015.

(3) Hiles, M.; Grossutti, M.; Dutcher, J. R. Classifying Formulations of Crosslinked Polyethylene Pipe By Applying Machine-Learning Concepts to Infrared Spectra. *J. Polym. Sci., Part B: Polym. Phys.* **2019**, *57*, 1255−1262.

(4) Grossutti, M.; Hiles, M.; D'Amico, J.; Wareham, W. C.; Morling, B.; Graham, S.; Dutcher, J. R. Quantifying Stabilizing Additive Hydrolysis and Kinetics Through Principal Component Analysis of Infrared Spectra of Cross-Linked Polyethylene Pipe. *Polym. Degrad. Stab.* **2022**, *200*, 109963.

(5) Grossutti, M.; D'Amico, J.; Quintal, J.; MacFarlane, H.; Quirk, A.; Dutcher, J. R. Deep Learning and Infrared Spectroscopy: Representation Learning with a β-Variational Autoencoder. *J. Phys. Chem. Lett.* **2022**, *13*, 5787−5793.

(6) Hakkarainen, M.; Albertsson, A.-C. Environmental Degradation of Polyethylene. *Adv. Polym. Sci.* **2004**, *169*, 177−200.

(7) Maria, R.; Rode, K.; Schuster, T.; Geertz, G.; Malz, F.; Sanoria, A.; Oehler, H.; Brüll, R.; Wenzel, M.; Engelsing, K.; Bastian, M.; Brendlé, E. Ageing Study of Different Types of Long-Term Pressure Tested PE Pipes By IR-Microscopy. *Polymer* **2015**, *61*, 131−139.

(8) Gardette, M.; Perthue, A.; Gardette, J. L.; Janecska, T.; Földes, E.; Pukánszky, B.; Therias, S. Photo- and Thermal-Oxidation of Polyethylene: Comparison of Mechanisms and Influence of Unsaturation Content. *Polym. Degrad. Stab.* **2013**, *98*, 2383−2390.

(9) Yang, R.; Liu, Y.; Yu, J.; Wang, K. Thermal Oxidation Products and Kinetics of Polyethylene Composites. *Polym. Degrad. Stab.* **2006**, *91*, 1651−1657.

(10) Costa, L.; Luda, M. P.; Trossarelli, L. Ultra High Molecular Weight Polyethylene—II. Thermal- and Photo-Oxidation. *Polym. Degrad. Stab.* **1997**, *58*, 41−54.

(11) Tidjani, A.; Watanabe, Y. Comparison of Polyethylene Hydroperoxide Decomposition Under Natural and Accelerated Conditions. *Polym. Degrad. Stab.* **1995**, *49*, 299−304.

(12) Cruz-Pinto, J. J. C.; Carvalho, M. E. S.; Ferreira, J. F. A. The Kinetics and Mechanism of Polyethylene Photo-Oxidation. *Angew. Makromol. Chem.* **1994**, *216*, 113−133.

(13) Wang, A. Y. T.; Murdock, R. J.; Kauwe, S. K.; Oliynyk, A. O.; Gurlo, A.; Brgoch, J.; Persson, K. A.; Sparks, T. D. Machine Learning For Materials Scientists: An Introductory Guide Toward Best Practices. *Chem. Mater.* **2020**, *32*, 4954−4965.

(14) Batra, R.; Dai, H.; Huan, T. D.; Chen, L.; Kim, C.; Gutekunst, W. R.; Song, L.; Ramprasad, R. Polymers For Extreme Conditions Designed Using Syntax-Directed Variational Autoencoders. *Chem. Mater.* **2020**, *32*, 10489−10500.

(15) Karande, P.; Gallagher, B.; Han, T. Y. J. A Strategic Approach to Machine Learning for Material Science: How to Tackle Real-World Challenges and Avoid Pitfalls. *Chem. Mater.* **2022**, *34*, 7650−7665.

(16) Trejo, O.; Dadlani, A. L.; De La Paz, F.; Acharya, S.; Kravec, R.; Nordlund, D.; Sarangi, R.; Prinz, F. B.; Torgersen, J.; Dasgupta, N. P. Elucidating the Evolving Atomic Structure in Atomic Layer Deposition Reactions with in situ XANES and Machine Learning. *Chem. Mater.* **2019**, *31*, 8937−8947.

(17) Xu, H.; Ma, S.; Hou, Y.; Zhang, Q.; Wang, R.; Luo, Y.; Gao, X. Machine Learning-Assisted Identification of Copolymer Microstructures Based on Microscopic Images. *ACS Appl. Mater. Interfaces* **2022**, *14*, 47157−47166.

(18) Park, Y.; Cho, K.; Kim, S. Performance Prediction of Hybrid Energy Harvesting Devices Using Machine Learning. *ACS Appl. Mater. Interfaces* **2022**, *14*, 11248−11254.

(19) Routh, P. K.; Liu, Y.; Marcella, N.; Kozinsky, B.; Frenkel, A. I. Latent Representation Learning for Structural Characterization of Catalysts. *J. Phys. Chem. Lett.* **2021**, *12*, 2086−2094.

(20) Burgess, C. P.; Higgins, I.; Pal, A.; Matthey, L.; Watters, N.; Desjardins, G.; Lerchner, A. Understanding Disentangling in β-VAE. **2018**, arXiv:1804.03599.

(21) Higgins, I.; Matthey, L.; Pal, A.; Burgess, C.; Glorot, X.; Botvinick, M.; Mohammed, S.; Lerchner, A. β-VAE: Learning Basic Visual Concepts with a Constrained Variational Framework. In *ICLR 2017*, 2016.

(22) D'Amico, J. Tracking the Effect of Accelerated Aging on Cross-Linked Polyethylene Pipe using Fourier Transform Infrared Microscopy. M.Sc. Thesis, University of Guelph, 2022.

(23) Demšar, J.; Curk, T.; Erjavec, A.; Gorup, Č.; Hočevar, T.; Milutinovič, M.; Možina, M.; Polajnar, M.; Toplak, M.; Starič, A.; Štajdohar, M. Orange: Data Mining Toolbox in Python. *J. Mach. Learn. Res.* **2013**, *14*, 2349−2353.

(24) Goodfellow, I.; Bengio, Y.; Courville, A. *Deep Learning*; MIT Press: Cambridge, 2016.

(25) Kingma, D. P.; Welling, M. Auto-encoding Variational Bayes. **2013**, arXiv:1312.6114.

(26) Abadi, M.; Agarwal, A.; Barham, P.; Brevdo, E.; Chen, Z.; Citro, C.; Corrado, G. S.; Davis, A.; Dean, J.; Devin, M.; Ghemawat, S.; Goodfellow, I.; Harp, A.; Irving, G.; Isard, M.; Jia, Y.; Jozefowicz, R.; Kaiser, L.; Kudlur, M.; Levenberg, J.; Mane, D.; Monga, R.; Moore, S.; Murray, D.; Olah, C.; Schuster, M.; Shlens, J.; Steiner, B.; Sutskever, I.; Talwar, K.; Tucker, P.; Vanhoucke, V.; Vasudevan, V.; Viegas, F.; Vinyals, O.; Warden, P.; Wattenberg, M.; Wicke, M.; Yu, Y.; Zheng, X. Tensorflow: Large-Scale Machine Learning on Heterogeneous Distributed Systems. **2016**, arXiv:1603.04467.

(27) Chollet, F. GitHub Repository, GitHub. 2015, https://github.com/fchollet/keras (last accessed April 6, 2023).

(28) Kingma, D. P.; Ba, J. Adam: A Method for Stochastic Optimization. **2014**, arXiv:1412.6980.

(29) Gulmine, J. V.; Akcelrud, L. FTIR Characterization of Aged XLPE. *Polym. Test.* **2006**, *25*, 932−942.

(30) Fairbrother, A.; Hsueh, H.; Kim, J.; Jacobs, D.; Perry, L.; Goodwin, D.; White, C.; Watson, S.; Sung, L. Temperature and Light Intensity Effects on Photodegradation of High-Density Polyethylene. *Polym. Degrad. Stab.* **2019**, *165*, 153−160.

(31) Zhang, Y.; Hou, Z.; Wu, K.; Wang, S.; Li, J.; Li, S. Influence of Oxygen Diffusion on Thermal Ageing of Cross-Linked Polyethylene Cable Insulation. *Materials* **2020**, *13*, 2056.

(32) Küpper, L.; Gulmine, J. V.; Janissek, P. R.; Heise, H. M. Attenuated Total Reflection Infrared Spectroscopy For Micro-Domain Analysis of Polyethylene Samples After Accelerated Ageing Within Weathering Chambers. *Vib. Spectrosc.* **2004**, *34*, 63−72.

(33) Jabarin, S. A.; Lofgren, E. A. Photooxidative Effects on Properties and Structure of High-Density Polyethylene. *J. Appl. Polym. Sci.* **1994**, *53*, 411−423.

(34) Satoto, R.; Subowo, W. S.; Yusiasih, R.; Takane, Y.; Watanabe, Y.; Hatakeyama, T. Weathering of High-Density Polyethylene in Different Latitudes. *Polym. Degrad. Stab.* **1997**, *56*, 275−279.

(35) Albertsson, A. C.; Barenstedt, C.; Karlsson, S. Susceptibility of Enhanced Environmentally Degradable Polyethylene to Thermal and Photo-Oxidation. *Polym. Degrad. Stab.* **1992**, *37*, 163−171.

(36) Beattie, J. R.; Esmonde-White, F. W. Exploration of Principal Component Analysis: Deriving Principal Component Analysis Visually Using Spectra. *Appl. Spectrosc.* **2021**, *75*, 361−375.

(37) Rowe, R. K.; Abdelaal, F. B. Antioxidant Depletion in High-Density Polyethylene (HDPE) Geomembrane with Hindered Amine Light Stabilizers (HALS) in Low-pH Heap Leach Environment. *Can. Geotech. J.* **2016**, *53*, 1612−1627.

(38) Beißmann, S.; Stiftinger, M.; Grabmayer, K.; Wallner, G.; Nitsche, D.; Buchberger, W. Monitoring the Degradation of Stabilization Systems in Polypropylene During Accelerated Aging Tests by Liquid Chromatography Combined with Atmospheric Pressure Chemical Ionization Mass Spectrometry. *Polym. Degrad. Stab.* **2013**, *98*, 1655−1661.

(39) Bertoldo, M.; Ciardelli, F. Water Extraction and Degradation of a Sterically Hindered Phenolic Antioxidant in Polypropylene Films. *Polymer* **2004**, *45*, 8751−8759.

(40) Nagy, K.; Epacher, E.; Staniek, P.; Pukánszky, B. Hydrolytic Stability of Phenolic Antioxidants and its Effect on Their Performance in High-Density Polyethylene. *Polym. Degrad. Stab.* **2003**, *82*, 211−219.

(41) Tátraaljai, D.; Vámos, M.; Orbán-Mester, Á.; Staniek, P.; Földes, E.; Pukánszky, B. Performance of PE Pipes Under Extractive Conditions: Effect of the Additive Package and Processing. *Polym. Degrad. Stab.* **2014**, *99*, 196−203.

(42) Reingruber, E.; Buchberger, W. Analysis of Polyolefin Stabilizers and Their Degradation Products. *J. Sep. Sci.* **2010**, *33*, 3463−3475.

(43) Krimm, S. C. Y. L.; Liang, C. Y.; Sutherland, G. B. B. M. Infrared Spectra of High Polymers. II. Polyethylene. *J. Chem. Phys.* **1956**, *25*, 549−562.

(44) Yu, W.; Azhdar, B.; Andersson, D.; Reitberger, T.; Hassinen, J.; Hjertberg, T.; Gedde, U. W. Deterioration of Polyethylene Pipes Exposed to Water Containing Chlorine Dioxide. *Polym. Degrad. Stab.* **2011**, *96*, 790−797.